Lift enhancement and drag reduction of lifting blades through the use of end-plates and detached end-plates

Thierry Villeneuve*, Matthieu Boudreau, Guy Dumas**

CFD Laboratory LMFN, Département de Génie Mécanique, Université Laval, Québec, Canada, G1V 0A6

Postprint, 2019 - Journal of Wind Engineering and Industrial Aerodynamics
Published version available online at: https://doi.org/10.1016/j.jweia.2018.12.006

Abstract

Three-dimensional steady-state RANS simulations of the flow around a stationary finite-span blade have been carried out. The analysis is directed toward the vorticity dynamics, the forces acting on the blade and their spanwise distributions when using end-plates or detached end-plates, namely end-plates that are not in contact with the blade tips. The objective is to understand the physics at play in the vicinity of the blade tips with an emphasis on the detached end-plates, as the use of such devices could be beneficial for optimizing the performance of vertical-axis turbines. This paper also aims at providing simple guidelines regarding the use of end plates and detached end-plates. The results show that the presence of detached end-plates leads to an important increase of the blade lift coefficient in addition to a significant reduction of its drag coefficient. This is explained by the fact that the detached end-plates modify the path of the vorticity lines shed by the blade, thus affecting the vorticity distribution and the resulting circulation along the blade. This work also shows that the forces on the blade are more sensitive to the dimensions of the detached end-plates in the transverse direction than to any other geometric parameter.

Keywords: Wing, Tip vortex, Vortex lines, Cross-flow turbine, Vertical-axis turbine, Flapping-foil turbine

1. Introduction

Over the past decades, the field of aviation has been the main motivation for the study of wingtip vortices [1, 2]. Indeed, many experimental and numerical studies have been directed toward the structure, the development and the decay of wingtip vortices in the near field of a wing [3, 4, 5, 6, 7, 8, 9, 10, 11, 12, 13, 14]. For example, Chow et al. [4] have provided detailed measurements of the turbulent structures that are essential to the fundamental understanding of the flow near a wingtip.

From a more practical perspective, it is well known that the 3D flow resulting from the wingtip vortices is responsible for a reduction of the lift coefficient and an increase of the drag coefficient of lifting wings. Consequently, much research effort has been devoted to the development of effective wingtip devices [15, 16, 17].

In spite of their success in aviation, such wingtip devices have received much less attention for wind and hydrokinetic turbine blade applications [18, 19, 20, 21], even if it has been shown that the tip losses associated with the three-dimensional flow around the blades can be very detrimental to the efficiency of various types of lift-driven cross-flow turbines [18, 22]. For example, Kinsey and Dumas [20, 23] have studied flapping-foil turbines and they have pointed out that the efficiency of such turbines is highly sensitive to the blade aspect ratio. Their numerical study has shown a considerable increase in the efficiency when end-plates were used, as it was also observed in the experimental work of Kim et al. [21].

*Corresponding author - thierry.villeneuve.2@ulaval.ca
**Corresponding author - guy.dumas@gmc.ulaval.ca

Several studies have also been devoted to the analysis of the flow field around another type of cross-flow turbine: the H-Darrieus vertical-axis turbine [18, 19, 24, 25, 26, 27, 28, 29]. It has been shown that the efficiency of three-dimensional vertical-axis turbines is significantly smaller than their idealized two-dimensional counterparts. More precisely, Gosselin et al. [18, 19] have shown that the efficiency ratio between an actual 3D turbine and its infinite-span analog (2D turbine) may be as small as 50% for blades having an aspect ratio of 7. To mitigate this drastic efficiency drop, the authors added simple end-plates to their turbine. However, because of the blade motion, the additional viscous drag generated by the end-plates results in an undesirable resistive torque at the turbine shaft. The added drag thus impairs the beneficial effect of the end-plates on the power extraction [18, 19].

For vertical-axis turbines, this suggests that end-plates that would not be moving with the turbine blades could be beneficial. In other words, the development of detached end-plates, i.e., stationary end-plates that are not in contact with the blade tips, could help to significantly increase the efficiency of H-Darrieus vertical-axis turbines by increasing the lift on the blades without adding an undesirable drag contribution.

As they are obviously irrelevant in the field of aviation, detached end-plates have not drawn much attention in the literature yet. The interaction between a blade tip and a solid surface in close proximity has been studied in the context of turbomachinery and axial fans [30, 31, 32, 33, 34, 35], but these works were performed in highly confined environments and the focus was mainly directed toward the understanding of the tip-leakage vortical flow and the underlying mechanisms for cavitation in the gap between the blade tip and the exterior casing of the machine.

An important phase in the development of such detached end-plates for wind and hydrokinetic turbine applications is the fundamental understanding of the physics at play in the vicinity of the blade tips when detached end-plates are used. As a first step, the present work aims at understanding the effect of using detached end-plates on a simplified case, namely a stationary lifting blade. The main objective consists in highlighting the physical mechanisms affecting the forces on the stationary blade when detached end-plates are present. More precisely, we focus on the vorticity dynamics with detached end-plates placed at various distances from the blade tips.

The methodology used to simulate the flow over the stationary blade is first presented in Section 2. Then, the forces and the flow over a blade with regular attached end-plates and with detached end-plates located a various distances from the blade tips are analyzed in Sections 3.1 and 3.2. Lastly, the impact of some geometrical characteristics of the detached end-plates are discussed and their effects on the forces and on the flow field are briefly presented in Section 3.3.

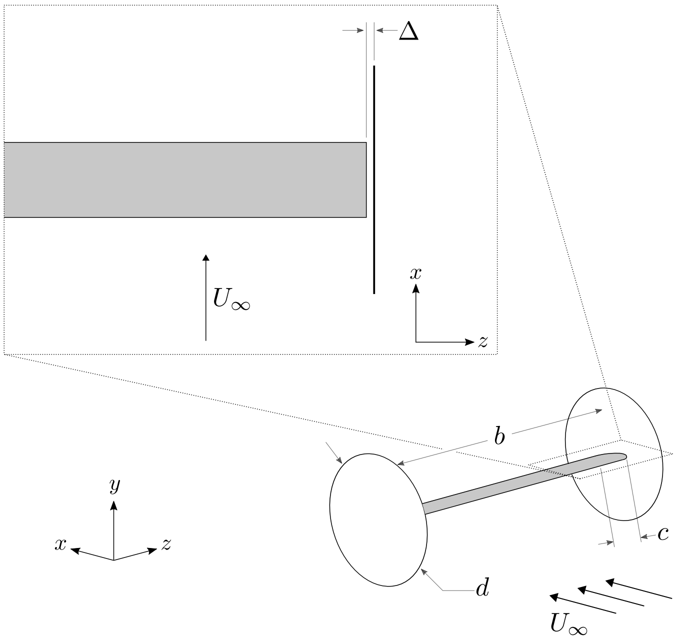

Figure 1: Outlines of the blade and the detached end-plates with the definition of some of the geometric parameters.

2. Methodology

2.1. Description of the studied problem

In this study, the geometry investigated is a straight rectangular blade (non-swept, non-tapered and non-twisted) that is formed with a NACA 0015 cross-section profile having a chord length c. The ratio between the blade span (b) and its chord length results in an aspect ratio b/c of 7.5. For all the parametric cases presented in this paper, the geometric angle of attack of the blade (α) is 10°.

The end-plates and detached end-plates used in the simulations are infinitely thin disks with a diameter (d) of $3c$. Note that this relatively large diameter is arbitrarily chosen and the effect of using different sizes and shapes of detached end-plates is discussed in Section 3.3. The end-plates are centered around the mid-chord point of the blade in both the streamwise and the transverse directions. The gap width (Δ) between the tips of the blade and the detached end-plates is varied between $\Delta/c = 0$, which represents an attached end-plate in contact with the blade tips and $\Delta/c = 1$, which is the largest gap width considered in this work. Figure 1 shows some of the main geometric parameters of the study.

The numerical simulations are carried out at a Reynolds number (Re_c) of 7.5×10^6, defined as:

$$\mathrm{Re}_c = \frac{U_\infty c}{\nu}, \tag{1}$$

where U_∞ is the freestream velocity and ν is the kinematic viscosity of the fluid.

The lift coefficient of the blade is given by:

$$C_L = \frac{L}{\frac{1}{2}\rho U_\infty^2\, bc}, \tag{2}$$

where L is the sum of the shear and the pressure force components acting on the blade in the y-direction (see Figure 1) and ρ is the density of the fluid.

Similarly, the drag coefficient is defined as:

$$C_D = \frac{D}{\frac{1}{2}\rho U_\infty^2\, bc}, \tag{3}$$

where D is the sum of the shear and the pressure forces in the x-direction (see Figure 1).

2.2. Numerics

The finite-volume Navier-Stokes solver from the Siemens® STAR-CCM+® software has been used to carry out the simulations [36]. Second-order schemes are used and a segregated approach with the SIMPLE algorithm is used for the pressure-velocity coupling. The simulations are carried out under incompressibility conditions. The steady-state RANS equations with the Spalart-Allmaras turbulence model are solved in fully-turbulent mode with rotation correction [9, 10, 37].

The computational domain used for the simulations is shown in Figure 3. Only one half of the blade is considered since a symmetry plane is used at the mid-span of the blade. The other lateral boundaries of the domain are also symmetry planes that are located far enough to ensure an essentially unconfined environment for the blade. The uniform velocity inlet boundary is located $100c$ upstream of the blade. At the inlet, a uniform turbulent viscosity ratio of $\nu_t/\nu = 0.2$ is imposed, as recommended by Spalart and Rumsey [38]. At the outlet located $200c$ downstream of the blade, a uniform static pressure of zero is imposed.

An overset mesh technique is used for the different parts of the mesh. Separate mesh regions (overset meshes) were made

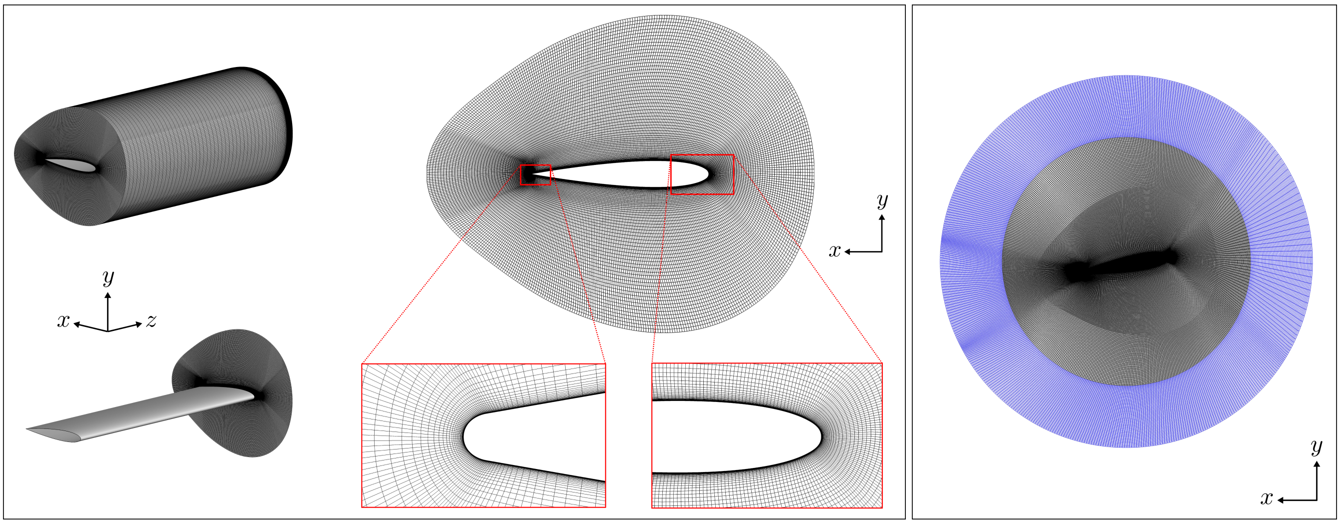

(a) Blade

(b) Detached end-plate

Figure 2: Illustrations of the local overset mesh of the blade from different views (a) and a cross-section view of the overset mesh of the detached end-plate (b). For the detached end-plate (b), note that the black region represents the infinitely thin end-plate and the blue region is the surrounding mesh.

for the half-blade and the end-plate, as shown in Figure 2. These two meshes are then imported over a background mesh in Star-CCM+®. At the beginning of the simulation, the meshes are merged and the cells from the background mesh that overlap those of the two overset meshes become inactive. This technique allows us to impose the desired angle of attack (10° for all the simulations in this study) and to change the gap width between the blade and the detached end-plate without reconstructing the entire mesh each time.

The mesh of the blade is an extrusion of the 2D structured mesh shown on the right of Figure 2a. The 2D NACA 0015 profile is composed of 450 nodes and the spanwise resolution along the middle part of the extruded blade results in 12 layers of cells per chord length and this spanwise resolution increases importantly near the tip of the blade. The resolution near the no-slip solid surfaces are chosen to ensure a dimensionless normal wall distance (y^+) around 1 with a maximum growth factor of 1.2. Similarly, the mesh of the end-plate is an extrusion of the 2D mesh shown in Figure 2b, where the black region represents the infinitely thin end-plate and the blue region is the surrounding mesh. The mesh of the blade and the mesh of the end-plate are created by extruding the same 2D mesh in the foil region. This technique ensures that the cells in the two zones have exactly the same size. As for the blade, the mesh of the detached end-plate is also composed of cells having dimensions that ensure a y^+ value of approximately 1 on both sides of the end-plate. Care has been taken to ensure that the resolution is approximately the same at the boundaries between all the different mesh regions. The background mesh is made of orthogonal cubic cells that have the same level of refinement as the overset meshes around the blade and the end-plate, and that become coarser as we move away from these zones. The blade and the detached end-plate meshes respectively contains 11M and 7M cells while the background mesh is composed of approximately 12M cells for a total of 30 million cells.

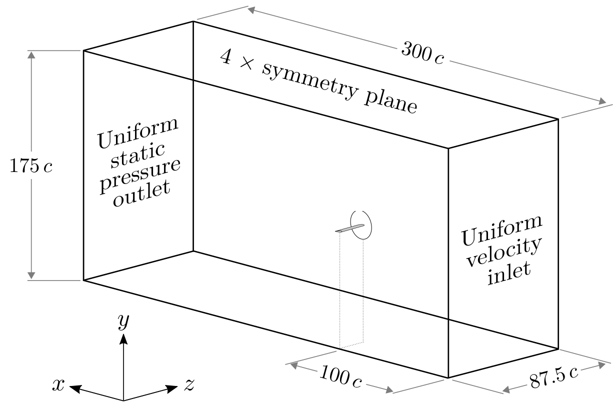

Figure 3: Computational domain and boundary conditions used in the numerical simulations. Note that the blade and the detached end-plate are scaled up by a factor of 4 for the sake of clarity.

2.3. Validation

Since a RANS methodology is used in the present study, it is important to mention that we are not focusing here on the fine details of the turbulence around the blade or in the wingtip vortex. We are rather interested in the global impacts of end-plates and detached end-plates on the forces acting on a blade and on the general flow field. In this context, RANS simulations are deemed adequate [40, 41].

In order to further validate the use of RANS simulations, the problem studied by Chow et al. [4, 39] has been reproduced numerically with the methodology used in the present work and the results have been compared to their experimental data. At different spanwise locations, they measured the surface pressure distribution around the NACA 0012 profile of the half-blade that they used at a Reynolds number of 4.6×10^6. In order

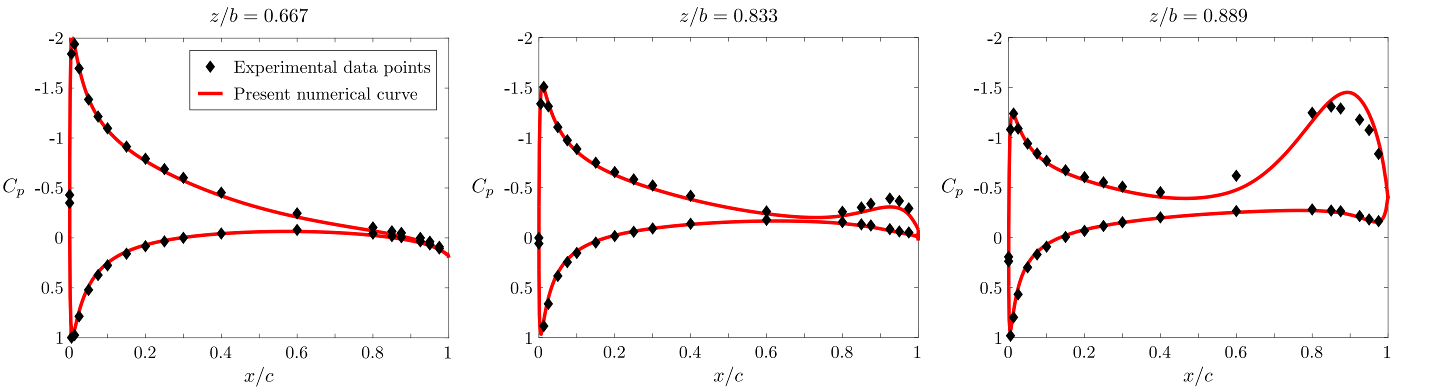

Figure 4: Comparison between the surface pressure coefficient distributions reported by Chow et al. [39] (black markers) and the distributions obtained with the actual numerical methodology (red curves) at three different spanwise locations: $z/b = 0.667$, $z/b = 0.833$ and $z/b = 0.889$.

to reproduce the results of this experiment, care has been taken to match the measured experimental velocity U/U_{ref} at the probe location reported by Churchfield and Blaisdell [40, 41]. Figure 4 shows the experimental pressure coefficient (C_p) reported by Chow et al. [39] and the results obtained numerically with the present methodology. As one can notice, the numerical results agree well with the experimental data points, especially at the $z/b = 0.667$ spanwise location. At $z/b = 0.833$ and $z/b = 0.889$, there are small discrepancies in the pressure distributions on the suction side of the blade near the trailing edge, at the location under the wingtip vortex. Nevertheless, the comparison clearly shows that the global forces on the blade can be adequately evaluated using the present RANS methodology.

The results presented in this paper were verified to be mesh-independent. A finer mesh for which the blade profile is composed of 675 nodes and a finer spanwise resolution of 20 layers of cells per chord length in the mid-span region has been made. With an equivalent refinement level in the end-plate mesh and in the background mesh, the refined mesh case is composed of approximately 38 million cells, compared to 30 million for base mesh case. Figure 5 shows the lift and the drag coefficient distributions over the entire span of a blade with detached end-plates at a gap width $\Delta/c = 0.015$ for the two meshes tested. The span of the half-blade simulated has been split into 25 sections and each marker corresponds to the forces measured on a given section of the blade span. These 25 points are then mirrored across $z/c = 0$ to obtain the symmetric distributions shown in Figure 5. Note that this discretization is not related to the mesh resolution which would be much finer, especially near the blade tips. The distributions shown by the black and the orange markers, which correspond to the base mesh and the refined mesh cases respectively, are very similar to one another. The relative difference on the lift coefficient is 0.2% while the relative difference is 0.7% for the drag coefficient, thus confirming that our base mesh resolution is adequate.

The sensitivity of the results to the turbulence model used has also been verified. The cyan markers in Figure 5 show the lift and the drag coefficient distributions along the spanwise direction of a blade with detached end-plates at $\Delta/c = 0.015$ using a $k-\omega$ SST turbulence model instead of the Spalart-Allmaras

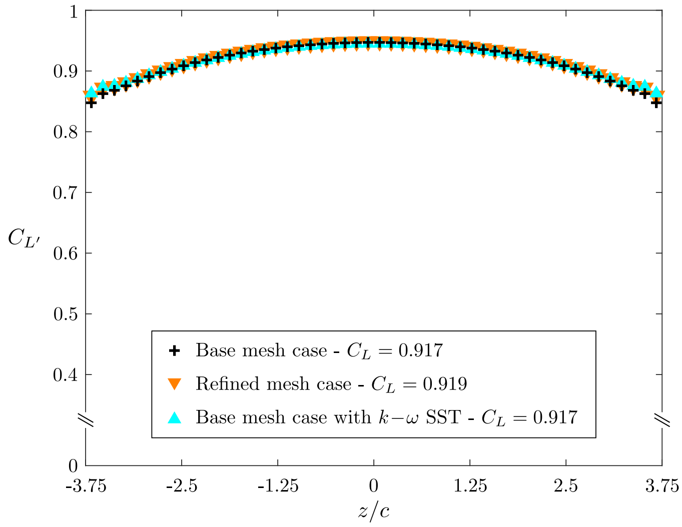

(a) Lift coefficient distributions

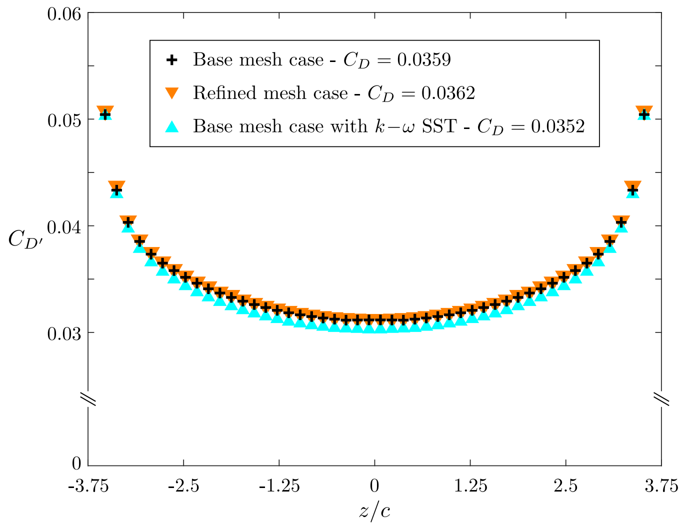

(b) Drag coefficient distributions

Figure 5: Section force coefficient distributions along the entire span of a blade with detached end-plates located at $\Delta/c = 0.015$ using two mesh refinement levels and two turbulence models.

model. The force distributions are very similar with the two turbulence models, especially for the lift force which is the main focus of this study.

Some unsteady simulations have also been conducted in order to assess the stationarity of the present RANS simulations. More precisely, a blade with detached end-plates at a gap width $\Delta/c = 0.015$ has been simulated using the base mesh and the Spalart-Allmaras turbulence model with a time step of $0.01c/U_\infty$. After initializing the solution with a uniform flow of U_∞ throughout the domain, the force coefficients converge toward the same values (within 0.2% difference) as those presented in Figure 5, hence confirming that the steady-state condition imposed in our calculation is adequate.

3. Results and discussion

3.1. Forces on a blade with detached end-plates

The objective of this section is to show the impact of using regular attached end-plates ($\Delta/c = 0$) and detached end-plates ($\Delta/c \neq 0$) on the forces acting on a stationary lifting blade.

3.1.1. Attached end-plates ($\Delta/c = 0$)

Serving as a baseline for the comparison with the detached end-plate cases presented in Section 3.1.2, Figure 6 shows the lift coefficient and the drag coefficient distributions on the span of a blade without end-plate (red markers) and on the span of a blade with attached end-plates ($\Delta/c = 0$, blue markers). As mentioned in Section 2.3, the markers in Figure 6 correspond to the forces measured on the different cross sections along the blade span.

Figure 6a shows that the main effect of the end-plates is to increase the lift coefficient near the tips of the blade. Indeed, even if there is a notable increase in the maximum section lift coefficient at the mid-span of the blade when end-plates are used ($C_{L',max} = 0.950$ compared to $C_{L',max} = 0.914$ for the blade without end-plate), the major difference between the two cases is observed near the blade tips. The lift coefficient of the blade with end-plates is $C_L = 0.928$, which is an increase of 16% in comparison with the blade without end-plate. Let us recall that the aspect ratio of the blade is $b/c = 7.5$. The impact of the end-plates on the lift coefficient is expected to be more important for smaller aspect ratios, while it is expected be less significant for larger aspect ratios.

In Figure 6b, one can see that the presence of end-plates leads to a reduction of the section drag coefficient at the mid-span of the blade and an even more important reduction near the tips compared to the blade without end-plate. Globally, the drag coefficient of the blade with end-plates is reduced by 15% in comparison with the blade without end-plate. It is also worth mentioning that the drag associated with the end-plates is smaller than the drag of the blade (approximately 12% of the blade drag for each end-plate).

3.1.2. Detached end-plates ($\Delta/c \neq 0$)

In Section 3.1.1, the lift and the drag coefficient distributions of a blade with and without end-plates have been presented. In this section, detached end-plates are considered and the objective is to see if a similar effect on the forces can be observed

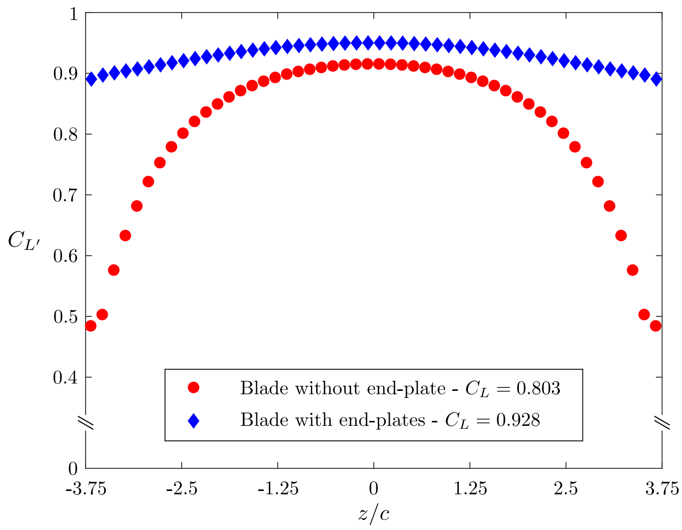

(a) Lift coefficient distributions

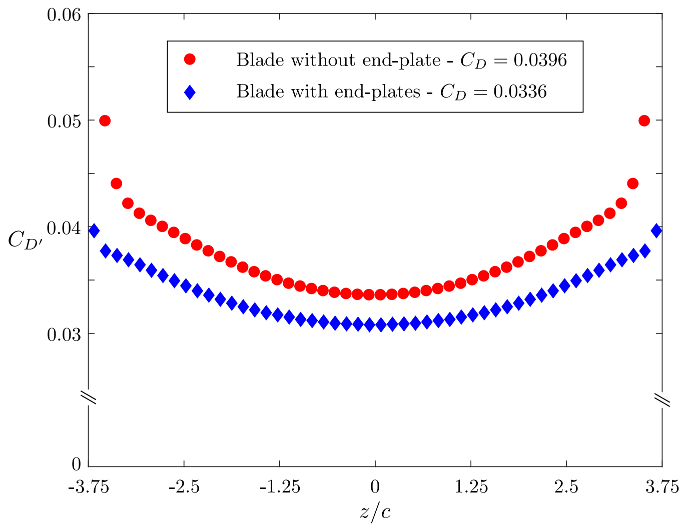

(b) Drag coefficient distributions

Figure 6: Section force coefficient distributions along the entire span of a blade with end-plates ($\Delta/c = 0$) in comparison with a blade without end-plate.

even if there is a gap between the blade tips and the detached end-plates.

Figure 7 shows the lift and the drag coefficients of the blade with detached end-plates for all the gap widths (Δ/c) considered. The point on the right of both curves corresponds to the blade without end-plate and the point on the left of the curves is for a gap width $\Delta/c = 0$, i.e., the blade with attached end-plates. All the other data points are distinct simulations of a blade with detached end-plates at various gap widths Δ/c. As shown in Figure 7, the presence of detached end-plates leads to a significant increase of the blade lift coefficient for the small gap widths and the effect becomes less important for the large gap widths. More precisely, the presence of detached end-plates at the smallest gap width simulated ($\Delta/c = 0.005$) leads to an increase in the lift coefficient of about 15% compared to the blade without end-plate. It is worth mentioning that the lift coefficient of the blade with detached end-plates at $\Delta/c = 0.005$ is only 1%

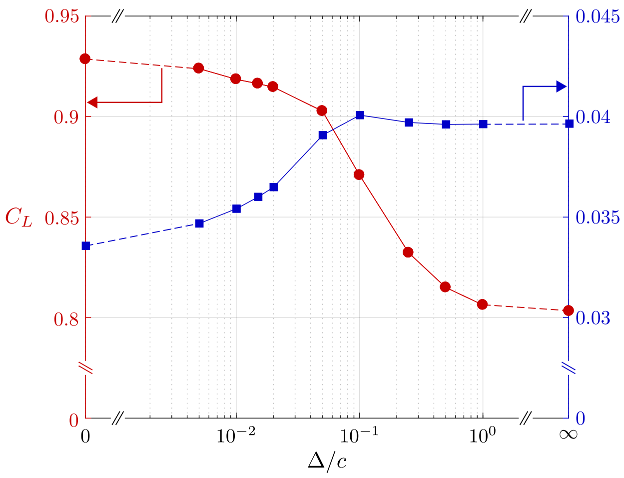

Figure 7: Lift coefficient (red markers) and drag coefficient (blue markers) of a blade with detached end-plates at various gap widths.

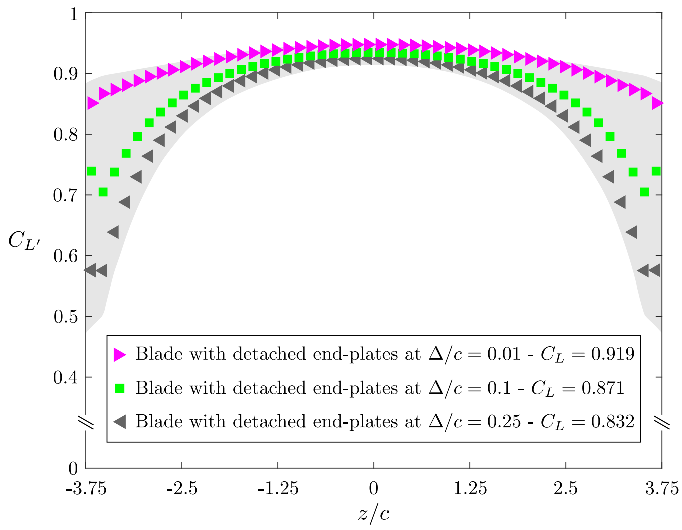

(a) Lift coefficient distributions

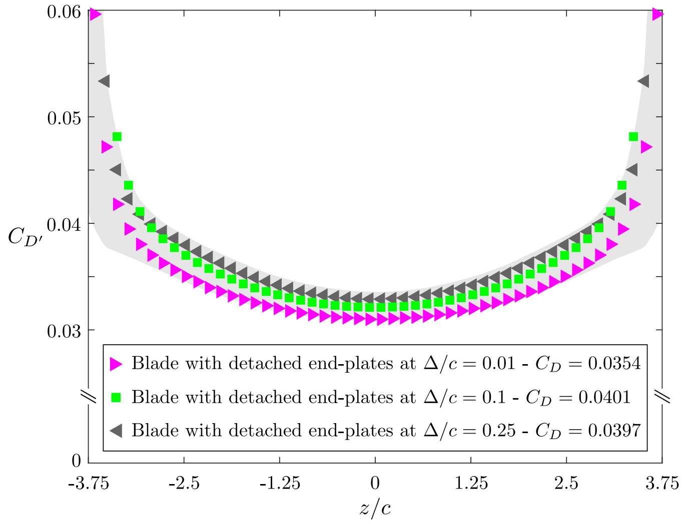

(b) Drag coefficient distributions

Figure 8: Section force coefficient distributions over the entire span of a blade with detached end-plates at three different gap widths. The gray zones correspond to the area contained between the red markers and the blue markers in Figure 6.

smaller than the one with attached end-plates ($\Delta/c = 0$), thus confirming that detached end-plates can be very efficient at increasing the lift on a blade. In Figure 7, one can notice that the drag coefficient of the blade is also significantly reduced for the small gap widths. For detached end-plates at $\Delta/c = 0.005$, the drag coefficient is indeed 13% smaller than the one of the blade without end-plate. As it can also be seen in Figure 7, there is a local maximum in the drag coefficient curve at a gap width $\Delta/c = 0.1$. This aspect is discussed in Section 3.2.2.

Figure 8 shows the lift coefficient and the drag coefficient distributions along the entire span of the blade with detached end-plates at three different gap widths. The gray zone in both plots of Figure 8 corresponds to the area contained between the red markers and the blue markers in Figure 6. In other words, the gray zones delimit the region between the two extreme cases, i.e., the lift and the drag coefficient distributions of the blade without end-plate and the blade with regular attached end-plates ($\Delta/c = 0$). Even for a relatively large gap width like $\Delta/c = 0.1$, one can notice in Figure 8a that the impact of the detached end-plates on the lift coefficient distribution is still significant. As the gap width decreases, the lift distribution tends toward the one of the attached end-plate case presented in Section 3.1.1 (blue markers in Figure 6a). Conversely, as the gap width increases, the distribution becomes closer to the one of a blade without end-plate. One can also notice that as the gap width decreases, the maximum section lift coefficient at the mid-span slightly increases, but again, it is near the tips of the blade that the impact of the gap width is the most important.

Figure 8b shows the drag coefficient distributions on the blade with detached end-plates at three different gap widths. As one could expect, the detached end-plates affect the drag coefficient distribution significantly near the blade tips. Moreover, the minimum section drag coefficient at the mid-span of the blade decreases as the gap width is reduced.

3.2. *Vorticity analysis*

Knowing that the presence of detached end-plates leads to an increase of the lift force and a reduction of the drag force on the blade, we are now addressing the question of how detached end-plates work. More specifically, the objective of this section is to discuss the physical mechanisms responsible for the increase of the blade lift when detached end-plates are used.

3.2.1. *Vorticity lines*

Analyzing the vorticity lines provides useful insights regarding the lift distribution on a lifting blade. To support this, Figure 9 shows a schematic representation of the vortex filaments around a lifting blade. As stated by the Kutta-Joukowski theorem [42], the section lift (L') can be evaluated using circulation diagnostics. Indeed, the theorem states that $L' = \rho U_\infty \Gamma$. The circulation ($\Gamma$), which varies along the blade span, can be determined by computing the vorticity flux passing through a given plane, similar to planes A, B and C in Figure 9, as follows:

$$\Gamma = -\iint_S \boldsymbol{\omega} \cdot \boldsymbol{n}\, \mathrm{d}S, \tag{4}$$

where $\boldsymbol{\omega}$ is the vorticity vector, S is the surface of the plane considered and $\boldsymbol{n}$ is a unit vector normal to the plane.

For a lifting blade, there is more vorticity contained in the boundary layer on the suction side than in the boundary layer on the pressure side of the blade. According to Helmholtz's second theorem [43], a vortex filament cannot end in the fluid. As a result, the vorticity in excess on the top surface necessarily has to be shed in the wake at some point along the span of the blade. The schematic vortex filaments that are disposed in a horseshoe shape in Figure 9 represent the behavior of this vorticity in excess on the suction side of the blade. As the lift decreases toward the blade tips, the circulation also decreases. This is related to the vortex filaments shed in the streamwise direction along the entire span of the blade. The circulation of each vortex filament actually corresponds to the spanwise variation of the blade lift. When the vortex filaments are shed in the streamwise direction, some circulation, and therefore some lift, is lost on the blade between the point where the vorticity line is shed and the tip of the blade.

This classic analysis of the vorticity lines can now be applied to the case of a blade with detached end-plates.

Recall that the vorticity lines are obtained similarly to streamlines, but using the vorticity vector field instead that the velocity vector field to integrate trajectories. Figure 10a shows two vorticity lines obtained from the simulation of the blade without end-plate, while Figure 10b shows four vorticity lines obtained from the numerical simulation of a blade with detached end-plates at $\Delta/c = 0.005$. Note that only one half of the blade is shown in Figure 10. In other words, the left end of the blade in Figure 10a and 10b corresponds to the blade mid-span.

It is important to note that the lines shown in Figure 10 are obtained numerically and that they are not schematic vortex filaments like those drawn in Figure 9. Moreover, each vortex line drawn in Figure 10 necessarily belongs to a vortex tube or a vortex filament which, according to Helmholtz theorem, is characterized by a constant circulation along its path. In the following discussion, we thus assimilate, without loss of generality or rigor, the vortex lines drawn in Figure 10 to actual vortex filaments of finite circulation. Therefore, the vortex lines of Figure 10 do portray the actual behavior of the vortex filaments near the tip of a blade with and without detached end-plates.

The vorticity lines colored in black in Figure 10 illustrate the fact that some of the vorticity in the top surface boundary layer is indeed connected to the vorticity in the bottom surface boundary layer. For a blade without end-plate (Figure 10a), one can see that the black vorticity line from the boundary layer on the blade pressure side simply curls around the tip of the blade and connects with the boundary layer on the suction side (traveling in the $+z$ direction on the bottom surface and in the $-z$ direction on the top surface of the blade). Considering this vortex line as a vortex filament, this means that the black filament does not contribute to the circulation around the blade since its positive and negative circulation contributions cancel each other out. When detached end-plates are used (Figure 10b), the black vorticity line shows a very interesting and important viscous interaction between the blade and the detached end-plate boundary layers. Indeed, one observes that the black filament underneath the blade (pressure side) goes all the way around the detached end-plate before coming back on the suction side of the blade, even if there is an open gap between the blade and the detached end-plate.

It becomes even more interesting when we analyze the other vorticity lines illustrated in red, blue and green in Figure 10. These vorticity lines come from the spanwise vorticity that is in excess in the boundary layer on the blade suction side. This excess in the suction side circulation, associated with the lift according to Kutta-Joukowski theorem, makes all those vortex filaments turn in the streamwise direction and carry the excess vorticity downstream of the blade. The red line in Figure 10a is a vorticity line that contributes to form the wingtip vortex. As one can expect, some of the vorticity lines in excess on the suction side of the blade with detached end-plates are also shed in the wake to form the wingtip vortex. The red vorticity line in Figure 10b is one of them. The main difference between the blade without end-plate and the one with detached end-plates is the presence of the blue and green vorticity lines.

The blue vorticity line from the suction side of the blade is

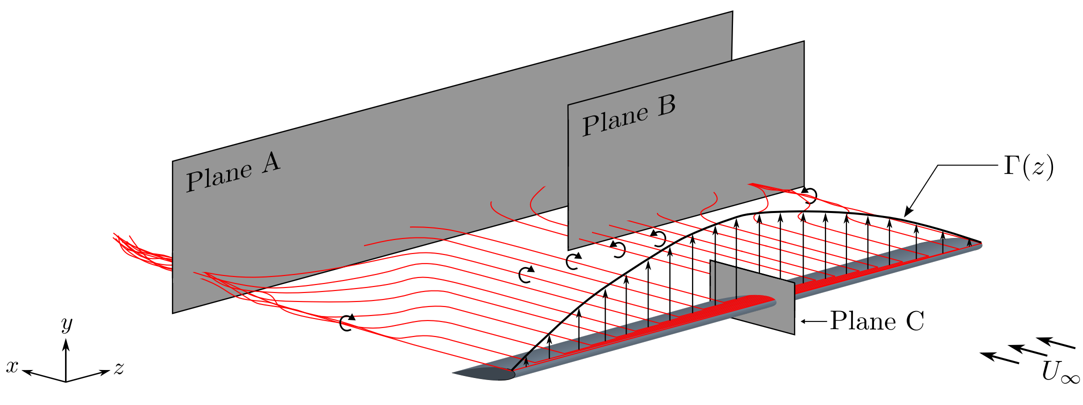

Figure 9: Schematic representation of the vortex filaments around a lifting blade without end-plate.

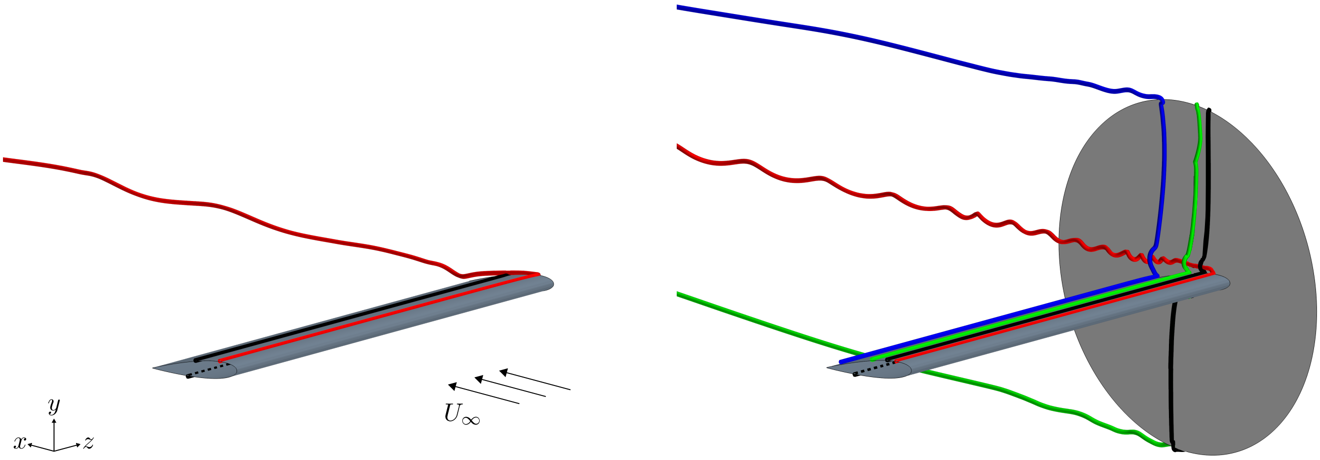

(a) Blade without end-plate

(b) Blade with detached end-plates ($\Delta/c = 0.005$)

Figure 10: Visualization of some vorticity lines (each one with his own color) obtained from the numerical simulations of a blade without end-plate (a) and a blade with detached end-plates at $\Delta/c = 0.005$ (b). Note that only half the span of the blade is visible and that the black lines are not visible on the pressure side of the blade, but they are illustrated in dashed lines near the mid-span.

shed in the wake at the upper extremity of the detached end-plate, while the green one goes around the back of the detached end-plate before being shed at its lower extremity. The critical point to note from Figure 10 is that some of the vorticity lines in excess on the suction side of the blade, that would normally be shed along the span of the blade or in the wingtip vortex for a blade without end-plate, can now follow a different path when detached end-plates are present. For a blade without end-plate, the fact that some vorticity lines are shed near the blade tips results in a decrease of the circulation, and thus, a decrease of the lift near the tips. When detached end-plates are used, some of these vorticity lines reach the blade tips while continuing their way on the detached end-plates. Therefore, the decrease in the circulation and the lift near the blade tips is less important. In other words, detached end-plates allow maintaining a more uniform circulation toward the tips, and thus, a more uniform loading (section lift) along the blade span. Note that this modification of the vorticity lines' paths is also responsible for the increase of the lift coefficient of the blade with regular attached end-plates ($\Delta/c = 0$). Indeed, the vorticity lines obtained for a blade with attached end-plates follow the same paths as those shown in Figure 10b.

For small gap widths, many vorticity lines are affected by the presence of the detached end-plates and many of them behave like the blue and green vorticity lines in Figure 10b. This is why Figures 7 and 8 show that the lift coefficient of the blade is increased when the detached end-plates are located close to the blade tips. Conversely, as the gap width is increased, the path of more vorticity lines remains unchanged compared to the blade without end-plate and the circulation and lift obtained are more similar to the blade without end-plate.

Figure 11 shows a volume rendering of the spanwise vorticity field around a blade without end-plate. As one can see, there is a rotational zone, thus a viscous zone, associated with the blade tip that exceeds the span of the blade. The rotational zone is

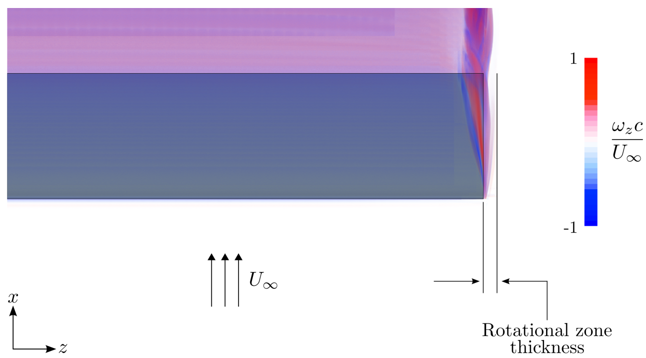

Figure 11: Top view of a volume rendering of the spanwise vorticity field around the tip of a blade without end-plate.

much larger than the thickness of a typical boundary layer. This vorticity around the tip is related to the connection between the boundary layers on the pressure side and on the suction side of the blade. A viscous interaction between the blade vorticity lines and the detached end-plate vorticity lines can thus occur when this rotational zone is in contact with the rotational zone associated with the boundary layers of the detached end-plate. If the gap width between the blade and the detached end-plate is such that the two rotational zones are not intersecting and are separated by a non-rotational region, the vorticity lines on the blade cannot interact with the detached end-plate and so, the lift of the blade tends toward the one of a blade without end-plate.

3.2.2. *Vorticity field*

In order to further highlight the physical mechanisms responsible for the increase of the blade lift coefficient when detached end-plates are used, it is interesting to analyse the vorticity distribution around the blade and the detached end-plates.

Figure 12 shows a volume rendering of the streamwise vorticity field around a blade with and without detached end-plates at various gap widths. Again, note that only one half of the blade is shown in Figure 12. For the blade without end-plate, most of the streamwise vorticity is contained in the wingtip vortex. For the blade with attached end-plates ($\Delta/c = 0$), the vorticity distribution is significantly different. The wingtip vortex is hardly visible, but there is an important amount of negative streamwise vorticity at the top and bottom extremities of the end-plate. For the blades with detached end-plates, vortex structures similar to those observed for the blade without end-plate and the blade with attached end-plates are visible, but the intensity of each vorticity region varies depending on the gap width. By looking at the vorticity fields shown in Figure 12, one can notice that for the four gap widths presented, there is always some negative streamwise vorticity shed on both the uppermost and lowermost extremities of the detached end-plates, as well as a positive streamwise vorticity region around the mid-height of the detached end-plates. One can conclude from Figure 12 that there are five different regions of non-zero streamwise vorticity around the blade and the detached end-plates. There are two regions associated with the blade, namely the blade tip region and the blade span region, and there are three other regions associated with the detached end-plates: the plate top region, the plate bottom region and the plate mid-height region.

For the small gap widths, the presence of the negative streamwise vorticity regions at the upper and lower extremities of the detached end-plates, observed in Figure 12, is coherent with the vorticity lines shown in Figure 10b. However, for the large gap widths (like $\Delta/c = 0.5$), where the rotational zones associated with the blade and the detached end-plates are separated by a non-rotational zone, the presence of the three streamwise vorticity regions on the detached end-plates may look surprising

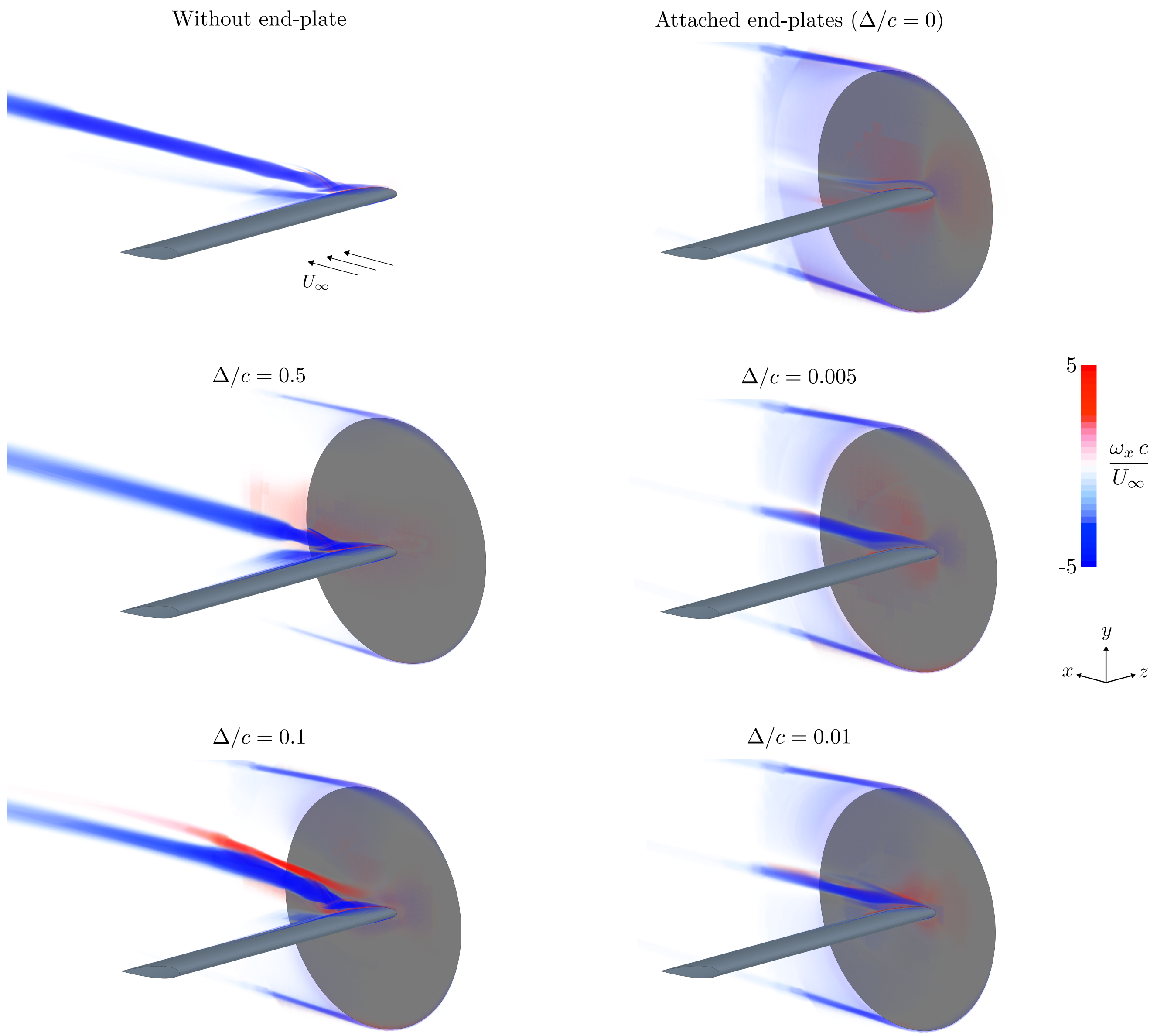

Figure 12: Volume renderings of the streamwise vorticity field around a blade with and without detached end-plates at different gap widths. Note that only half the span of the blade is shown in these visualizations. The gap width is increasing in the clockwise direction.

since there is no viscous interaction between the vorticity lines on the blade and on the detached end-plates. This can be explained by looking at the forces in the z-direction experienced by the detached end-plates. Indeed, the flow field is affected by the presence of the blade. In addition to being deviated, the flow is accelerated on the suction side of the blade and is slowed down on its pressure side. As a result, the detached end-plates do experience pressure forces in the z–direction (thus a lift in the z-direction). To illustrate that phenomenon, Figure 13 shows the local distribution of the force coefficient in the z-direction ($C_{z'}$) on a transverse line on the detached end-plate aligned with the mid-chord point of the blade for gap widths $\Delta/c = 0.5$ and $\Delta/c = 0.05$. On the upper portion of the detached end-plates ($y > 0$), there is a force directed toward the blade because of the suction above the blade and because of the presence of the wingtip vortex. Conversely, because of the higher pressure zone on the blade pressure side, the lower portion of the detached end-plates ($y < 0$) experiences a force directed away from the blade. Since the detached end-plates experience such forces in the z-direction, there necessarily are vortex filaments that are shed in the streamwise direction from the detached end-plates boundary layers. The three streamwise vorticity regions visible on the detached end-plates shown in Figure 12 are therefore related to these forces in the z-direction.

Similarly to Figure 9 that showed the vortex filaments in excess on the suction side of a lifting blade without end-plate, Figure 14 is a simplified illustration of the vortex filaments in excess around a detached end-plate at a large gap width. Since the upper portion of the detached end-plate experiences a force in the z-direction directed toward the blade (see red curve in Figure 13), there is some vorticity in excess in the boundary layer of the detached end-plate on the side facing the blade tip. That vorticity has to be shed in the wake at the upper extremity and at the mid-height of the detached end-plate due to the change of sign of $C_{z'}$, resulting in a negative streamwise vorticity region at the upper extremity and a positive streamwise vorticity region at mid-height, as observed in Figure 14. Conversely, for the lower portion of the detached end-plate, since the spanwise force is directed away from the blade, the vorticity in excess is located on the outer side of the detached end-plate. When this vorticity in excess is shed in the wake, it leads to a negative streamwise vorticity region at the bottom extremity and a positive streamwise vorticity region at the mid-height of the detached end-plate.

It is worth mentioning that when we refer to positive and negative streamwise vorticity, it is only applicable to the detached end-plates located to the right of the blade from a front view (those that are visible in Figure 12), as well as the right half of the blade. If we would look at the other detached end-plate and at the left half of the blade, the sign of the streamwise vorticity regions would be reversed.

Based on these observations, we can examine the intensity of each of the streamwise vorticity regions around the blade. Since the lift at any given section of the blade can be evaluated using circulation diagnostics, it is insightful to know where the streamwise vorticity is shed on the blade and which of the vorticity regions are dominant for the different gap widths of detached end-plates simulated.

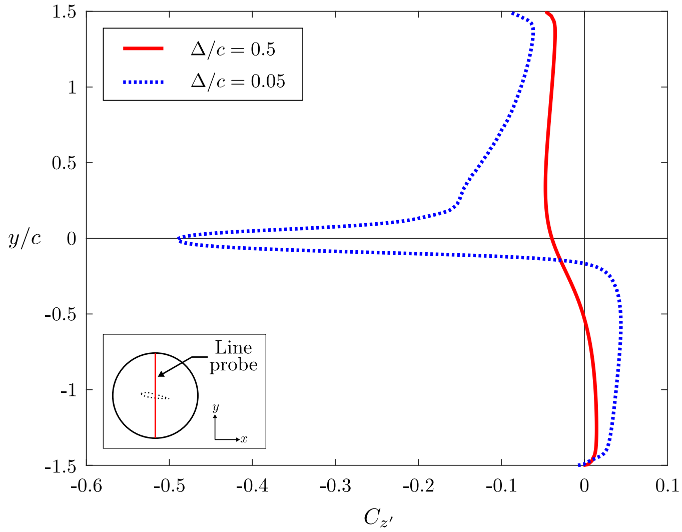

Figure 13: Local force coefficient (pressure force in the z-direction) distribution on a line located at the maximum height position on a detached end-plate for two different gap widths.

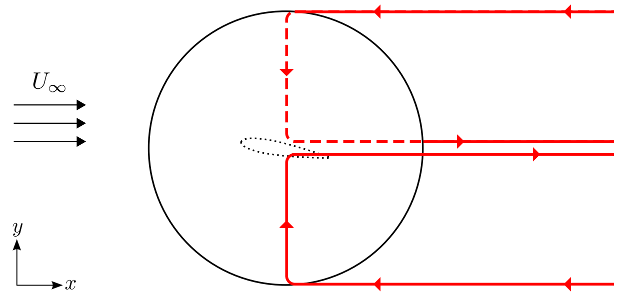

Figure 14: Schematic representation of the vortex filaments in excess around a detached end-plate at large gap widths. The dashed line represents the part of a vortex filament that is located behind the detached end-plate from this viewpoint.

For the five different vorticity regions that have just been discussed (the blade tip vorticity ①, the blade span vorticity ②, the plate top and bottom vorticity ③ and ④ and the plate mid-height vorticity ⑤), their respective contribution to the total circulation is assessed. The circulation of each of the five vorticity regions is measured for all the gap widths simulated on a plane perpendicular to the x-axis located at the trailing edge of the blade using Equation (4). For example, Figure 15 shows contours of the streamwise vorticity field at the trailing edge of a blade with detached end-plates at a gap width arbitrarily chosen at $\Delta/c = 0.05$ and each of the vorticity regions considered are identified. Figure 16 presents the dimensionless circulation associated with each vorticity region shown in Figure 15 as a function of the gap width.

The gray curve in Figure 16 shows the total circulation on the measurement plane at the trailing edge of the blade. As one can notice, the total circulation, corresponding to the blade mid-span circulation, does not vary much with the gap width and is not significantly affected even for the blade without end-plate. There is a slight increase in the total circulation as the gap width

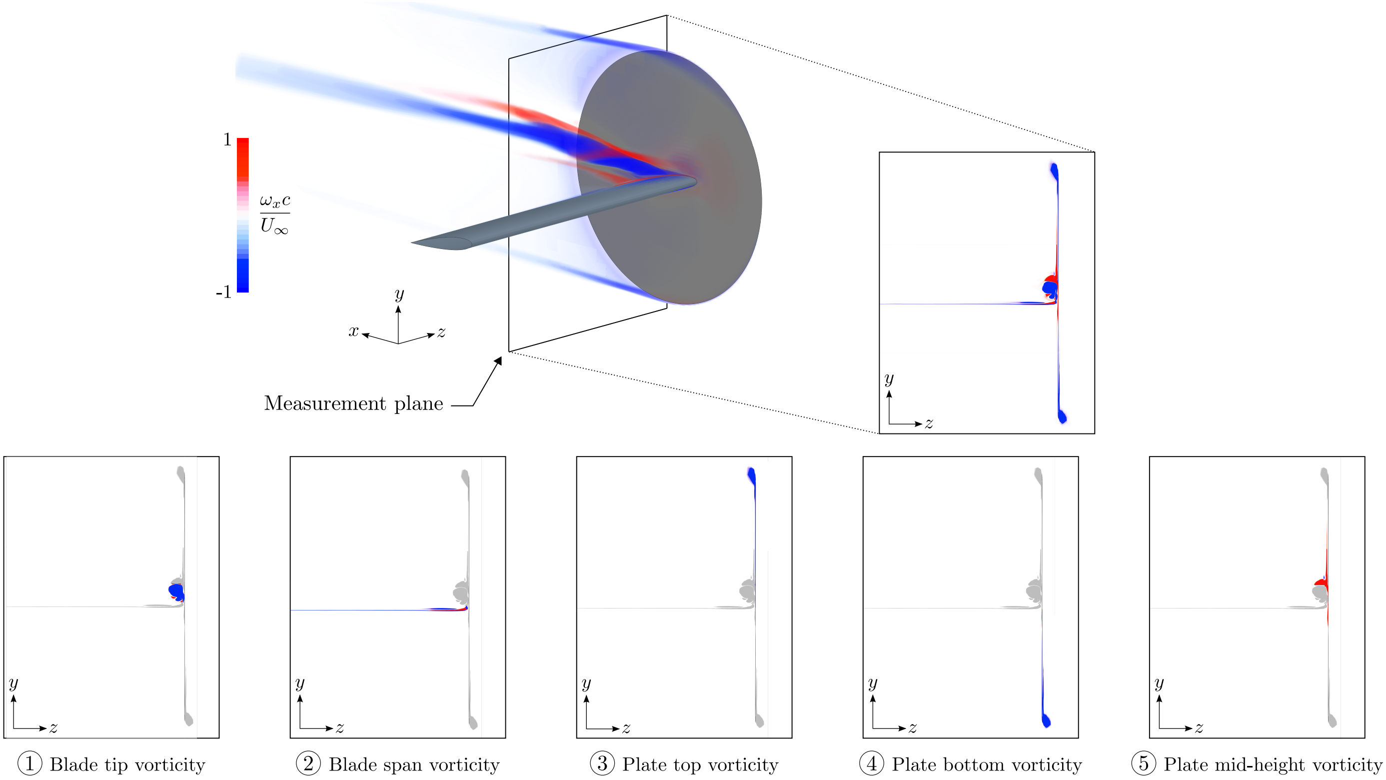

Figure 15: Contours of the streamwise vorticity field shown on a plane perpendicular to U_∞ at the trailing edge of a blade with detached end-plates at a gap width $\Delta/c = 0.05$.

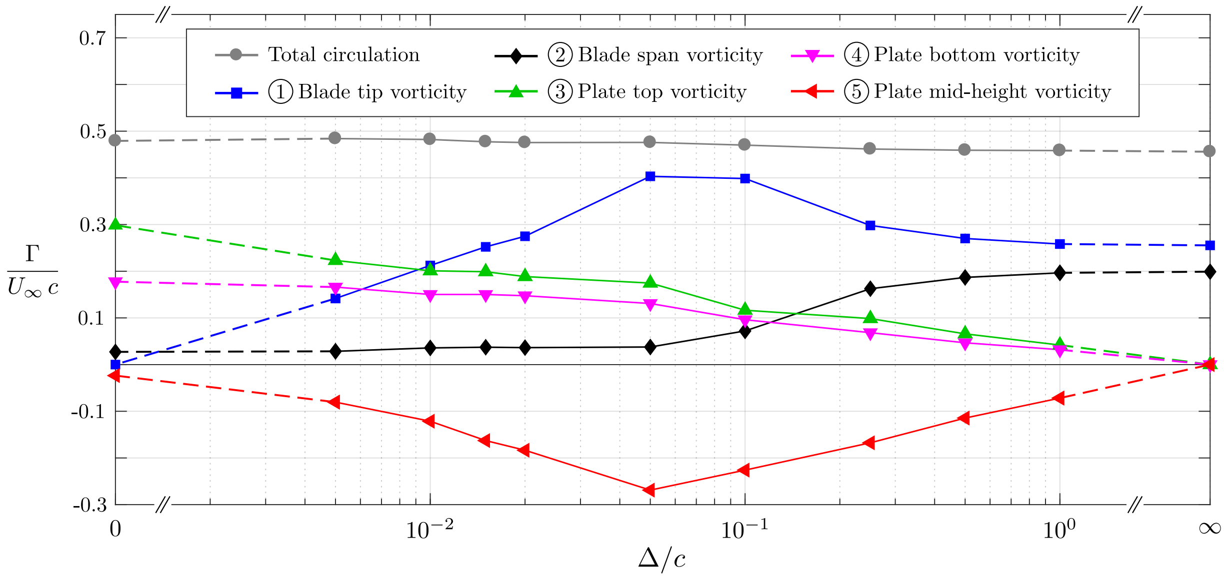

Figure 16: Dimensionless circulation associated with each of the vorticity regions identified in Figure 15 for the different gap widths simulated.

is reduced, which is coherent with the fact that the maximum section lift coefficient at the mid-span also slightly increases as the gap width becomes smaller, as shown in Figures 6 and 8. The sum of the five other curves is equal to the total circulation.

The green 3 and magenta 4 curves respectively represent the circulation of the vorticity regions at the upper and lower extremities of the detached end-plates. Obviously, for the blade without end-plate on the right of the plot, the circulation of these two regions is equal to zero. Then, as the gap width is reduced from $\Delta/c = 1$, the circulation of both the plate top and the plate bottom vorticity increases until the detached end-plates reach the blade. As the gap width is reduced, the forces in the z-direction experienced by the detached end-plates become more important. This implies that more vorticity is contained in the detached end-plate boundary layers, thereby suggesting an increased potential of interaction between the blade vorticity lines and the detached end-plate vorticity lines. In other words, the viscous interaction between the blade vorticity lines and the detached end-plate vorticity lines is strongly associated with the forces and the vorticity in the detached end-plate boundary layers.

For every gap width simulated, the circulation of the plate top vorticity is larger than the circulation of the plate bottom vorticity. Given the flow field caused by the presence of the blade, the forces in the z-direction on the detached end-plates are larger on their upper part than on their bottom part, as shown in Figure 13. Therefore, it makes sense to find that a larger circulation is associated with the upper part of the detached end-plate in comparison with the bottom part.

The black curve ② in Figure 16 represents the circulation associated with the vorticity that is shed along the span of the blade. For small gap widths, less circulation is shed on the blade span because of the strong viscous interaction between the vorticity lines on the blade and on the detached end-plates. Therefore, the lift coefficient distribution on the blade span is more uniform. Conversely, the circulation associated with the vorticity shed on the blade span becomes larger as the gap width is increased.

The blue ① and the red ⑤ curves in Figure 16 respectively show the circulation of the blade tip vorticity and the plate mid-height vorticity for the different gap widths. As one can notice, the two curves show a similar trend, but with opposite signs. For the blade without end-plate, the blade tip vorticity region has a dimensionless circulation of 0.26 and the plate mid-height vorticity is obviously zero. From the largest gap widths, the circulation associated with both these vorticity regions increases in absolute value as the gap width decreases until a gap width of approximately $\Delta/c = 0.05$. For smaller gap widths, the circulation of both these two vorticity regions (① and ⑤) starts to decrease in absolute value as the gap width further decreases. Dreyer et al. [32, 33] also noticed a similar trend in the circulation associated with the blade tip vorticity in their experimental study of the wingtip vortex in the near-field of a blade located close to a wall.

For the large gap widths ($\Delta/c \gtrsim 0.1$), it is interesting to note that the increase of the blade tip circulation balances the decrease of the blade span circulation as the gap width is reduced. Consequently, the circulation of the plate mid-height vorticity is equal to the sum of the circulation associated with the plate top and the plate bottom vorticity regions. This confirms that there is no viscous interaction between the blade and the detached end-plates for these large gap widths. However, for the small gap-widths ($\Delta/c \lesssim 0.05$), the viscous interaction between the vorticity lines on the blades and those on the detached end-plates results in a reduction of the circulation associated with both the plate mid-height and the blade tip circulation when the gap width further decreases and the sum of the circulation of the three vorticity regions on the detached end-plate does not equal to zero.

Therefore, for the small gap widths ($\Delta/c \lesssim 0.05$), the viscous interaction between the vorticity lines on the blade and on the detached end-plates results in an increase of the blade lift coefficient as the gap width decreases. For the large gap widths ($\Delta/c \gtrsim 0.1$), there is no interaction between the vorticity lines on the blade and the detached end-plates. It suggests that the detached end-plates rather realign the flow field near the blade tips, i.e., it reduces the local deviation of the flow in the $z-$direction near the tips of the blade. In Figure 16, the decrease of the blade span circulation (②) and the increase of the blade tip circulation (①) as the gap width decreases between $\Delta/c = 1$ and $\Delta/c = 0.1$ supports this hypothesis. Indeed, a more 2D flow along the blade span would result in less circulation shed along the blade span, and consequently, more circulation shed at the blade tip.

Moreover, Figure 16 also explains the local maximum in the drag coefficient curve that is visible in Figure 7 at a gap width $\Delta/c = 0.1$. The downwash induced by the intense tip vortices at $\Delta/c = 0.1$ is responsible for an increased section drag coefficient near the blade tips (see green markers in Figure 8b). Therefore, at $\Delta/c = 0.1$, the important tip vortices cause a downwash distribution on the blade that results in a drag coefficient that is larger than the drag coefficient of the blade without detached end-plate.

3.3. Geometric parameters of the detached end-plates

Following the previous discussion, it is worthwhile to analyze the impact of some geometric parameters of the detached end-plates on the blade lift and drag coefficients. For a given gap width, arbitrarily chosen at $\Delta/c = 0.015$, different geometries of detached end-plates have been simulated and these geometries are presented in Figure 17. It is important to note that the objective here is not to optimize the shape of the detached end-plates, but to differentiate the effects of different geometric factors. It is also worth mentioning that the analysis of the geometric parameters is made for detached end-plates, but the trends and the conclusions would be the same for attached end-plates in contact with the blade tips ($\Delta/c = 0$).

First, a blade with a square-shaped detached end-plate, as shown by geometry *A* in Figure 17, having streamwise and transverse dimensions equal to the diameter of the circular detached end-plates from the previous sections has been simu-

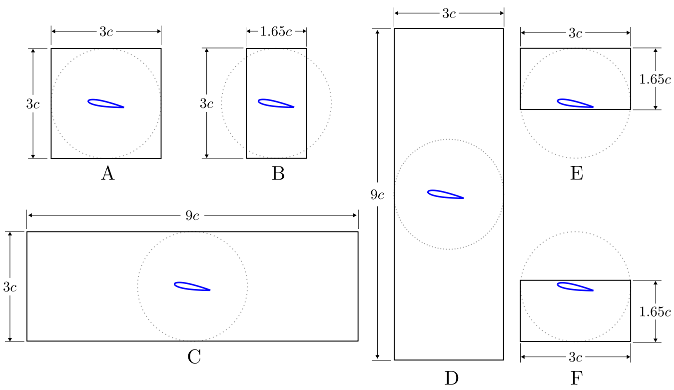

Figure 17: Outlines of the different geometries of detached end-plates tested. The dashed circles correspond to the geometry of the circular detached end-plates used in the previous sections.

lated. The results for the lift and the drag coefficients of the blade as well as their spanwise distributions are similar to those presented in Section 3.1.2 where equivalent round detached end-plates were used. The difference in the lift coefficient of the blade between the circular and the square-shaped detached end-plates is 0.3% while the drag coefficient differs by 0.8%. Using this square-shaped geometry as a reference, we can now see the impact of the streamwise and transverse dimensions of the detached end-plates by comparing it to rectangular detached end-plates.

Figure 18 shows the lift and the drag coefficient distributions over the entire span of a blade with detached end-plates having the geometries *A*, *B*, *C* and *D* shown in Figure 17. Note that the results obtained with the circular detached end-plates from the previous sections have also been included in Figure 18 for comparison purposes. As one can notice, increasing the streamwise dimensions of the detached end-plates (geometry *C*) does not considerably affect the lift and the drag coefficient distributions. It it not surprising considering that these distributions are affected by the interaction of the blade vorticity lines with the detached end-plate vorticity lines. As discussed previously, the potential of interaction is related to the force in the z-direction acting on the detached end-plates. When the streamwise dimensions of the detached end-plates are increased, the load on them is not significantly altered. Therefore, one does not expect a stronger interaction between the vorticity lines from the blade and those from the detached end-plates when the streamwise dimensions are increased. Moreover, Figure 18 shows that even the detached end-plates having the geometry *B* in Figure 17 leads to similar lift and drag coefficients as those obtained with the geometries *A* and *C*.

However, results from Figure 18 clearly illustrates that varying the transverse dimensions of the detached end-plates (geometry *D*) has a very important impact on the lift and drag coefficients. This significant increase of the lift and reduction of the drag can be explained by the fact that increasing the transverse dimensions of the detached end-plates is leading to a more loaded detached end-plate in the $z-$direction, and therefore to a stronger interaction between the vorticity lines on the blade and the detached end-plates. From a pressure-velocity point of view, we can say that if the streamwise vorticity shed at the extremities of the detached end-plates is moved further away from the tip of the blade by increasing the transverse dimensions of the detached end-plates, it reduces the downwash at the blade, therefore increasing the lift coefficient and reducing the drag coefficient. Based on these results, it is important to note that if one wants to design detached end-plates, the emphasis should be on the transverse dimensions of the end-plates more than on their streamwise dimensions.

Knowing that the transverse dimensions of the detached end-plates are a crucial geometric parameter, it is interesting to evaluate the impact of the symmetry of the transverse length of the detached end-plates with respect to the position of the blade. To investigate that, simulations have been carried out to compare the lift and the drag coefficient distributions on a blade with detached end-plates of geometries *A*, *E* and *F* from Figure 17.

As shown in Figure 19, the half-height detached end-plates of geometries *E* and *F* lead to a smaller increase in the lift coefficient and a smaller reduction of the drag coefficient than the square-shaped or circular detached end-plates. It is not surprising considering what has just been discussed. The half-height detached end-plates are less loaded than the other ones, therefore the interaction between the blade vorticity lines and the detached end-plate vorticity lines is weaker. Again, from a pressure-velocity point of view, all the vorticity associated with the extremities of the detached end-plates contributes to the reduction of the downwash at the blade in the case of symmetric detached end-plates. However, in the case of the half-height detached end-plates located above the blade for example (geometry *E*), only the vorticity associated with the upper extremity of the detached end-plates contributes to the reduction of the downwash at the blade. Moreover, the fact that the load and the circulation associated with the vorticity at the upper extremity

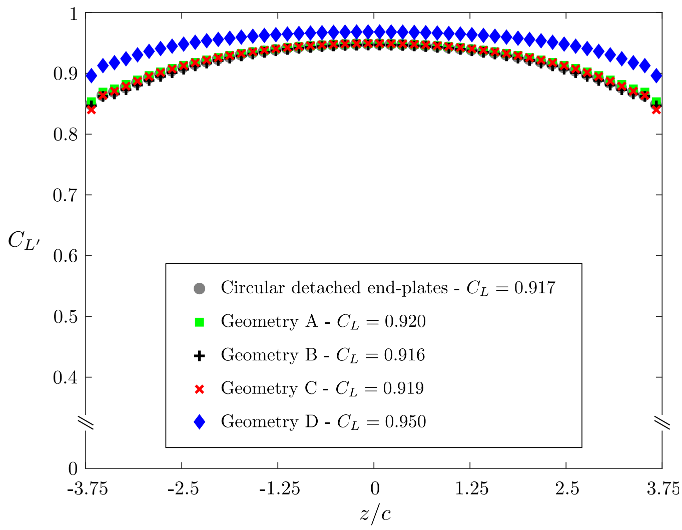

(a) Lift coefficient distributions

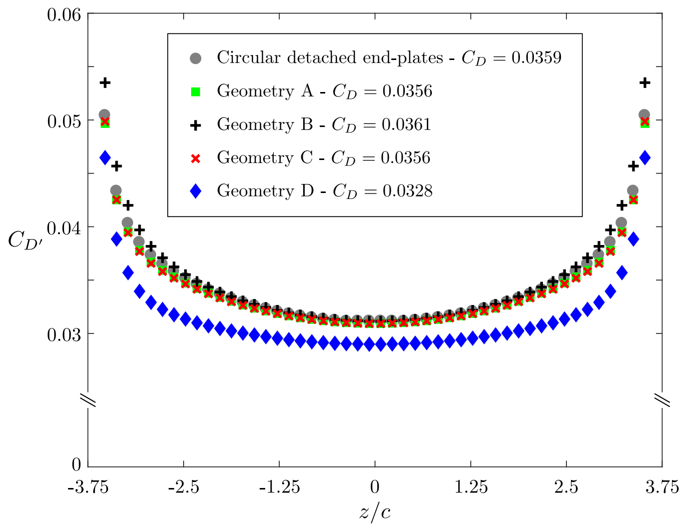

(b) Drag coefficient distributions

Figure 18: Section force coefficient distributions over the entire span of a blade with different geometries of detached end-plates (see Figure 17) at a gap width $\Delta/c = 0.015$.

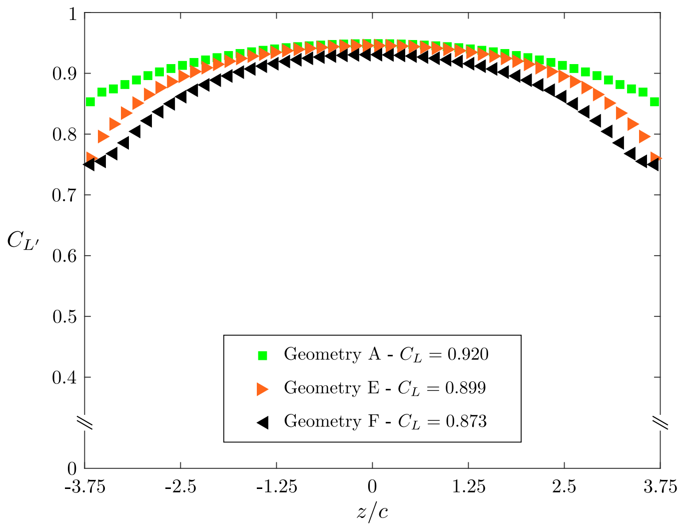

(a) Lift coefficient distributions

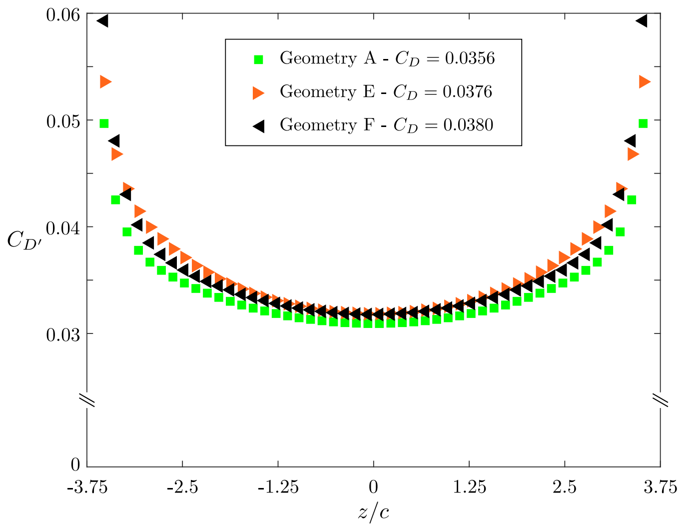

(b) Drag coefficient distributions

Figure 19: Section force coefficient distributions over the entire span of a blade with different geometries of detached end-plates (see Figure 17) at a gap width $\Delta/c = 0.015$.

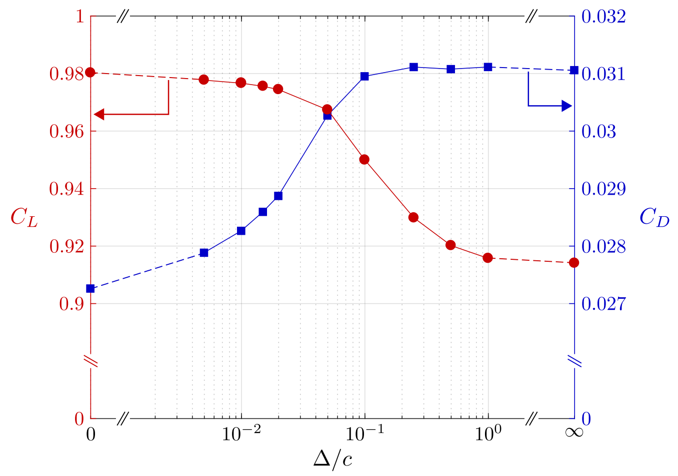

Figure 20: Lift coefficient (red markers) and drag coefficient (blue markers) of a blade having an aspect ratio $b/c = 15$ with detached end-plates at various gap widths.

of the detached end-plates are more important than those at the bottom extremity (see Figures 13 and 16) explains that the half-height detached end-plates located above the blade (geometry *E*) are slightly better in terms of the lift and the drag coefficients than the half-height detached end-plates located below the blade (geometry *F*). Consequently, if one wants to use detached end-plates, it would be better to design them so that they extend beyond the blade, both above and below it.

3.4. Generality of the results

In order to ensure the generality of the conclusions presented in this paper, some simulations have been carried out to investigate the effect of the blade aspect ratio (b/c), the angle of attack of the blade (α) and the Reynolds number (Re_c).

Regarding the blade aspect ratio, simulations have been conducted for a blade having an aspect ratio $b/c = 15$. Figure 20 shows the lift and the drag coefficients of the blade having an aspect ratio $b/c = 15$ for all the gap widths simulated. As one can see, the results show similar trends as those obtained with the blade having an aspect ratio of 7.5. However, the impacts of the detached end-plates on the lift and the drag coefficients are slightly less important. Indeed, when $b/c = 15$, since the spanwise distributions of the lift and drag coefficients are more uniform, i.e., the impact of the downwash is a little more confined near the tips of the blade compared to the blade with the aspect ratio $b/c = 7.5$, the impact of the detached end-plates on the lift and the drag coefficient distributions is reduced. More quantitatively, the lift coefficient of a blade having an aspect ratio $b/c = 15$ with attached end-plates ($\Delta/c = 0$) is increased by about 7% compared the blade without end-plate. This increase was about 16% for the blade having an aspect ratio $b/c = 7.5$. Nevertheless, it is important to note that the presence of detached end-plates still increases the lift coefficient of the blade and reduces its drag coefficient. Furthermore, the conclusions about the physics at play made in the previous sections are still valid.

Simulations have also been conducted for a blade at an angle of attack $\alpha = 5°$. Similarly, it has been found that the impact of the detached end-plates is slightly less significant on the lift and drag coefficients, but again, the conclusions from previous sections are still true.

Regarding the impact of the Reynolds number Re_c, simulations have been carried out for a blade with detached end-plates at a gap width $\Delta/c = 0.01$ at Reynolds numbers of 7.5×10^5 and 7.5×10^7. Results regarding the lift coefficient and drag coefficient distributions are reported in Figure 21. As it can be seen, the impact of the detached end-plates on the blade lift and drag coefficients become more important as the Reynolds number is increased. An increase in the Reynolds number results in an increased lift coefficient for the blade without end-plate, hence increasing the amount of vorticity in excess in the boundary layer on the top surface of the blade and resulting in a more important load on the detached end-plates. Thus, it leads to a stronger potential of interaction between the blade vorticity

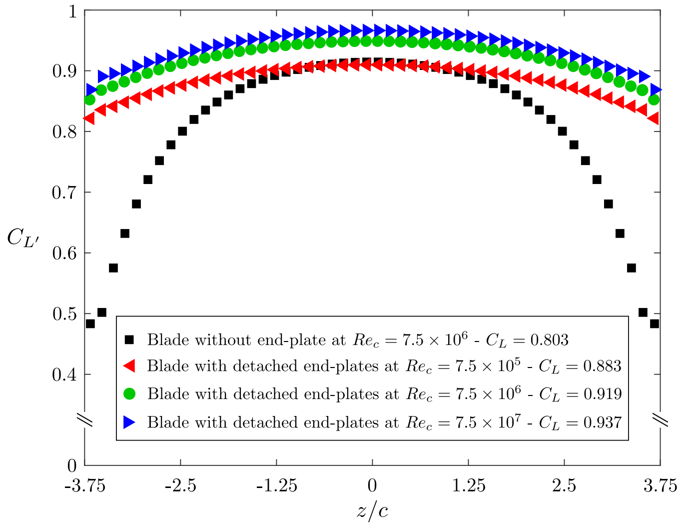

(a) Lift coefficient distributions

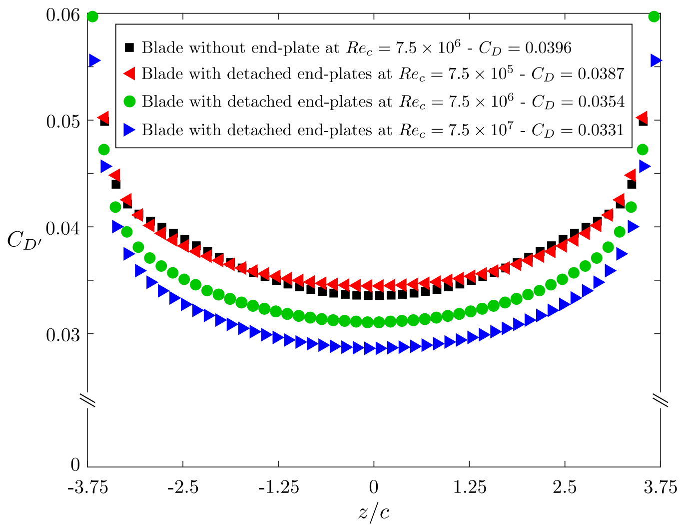

(b) Drag coefficient distributions

Figure 21: Section force coefficient distributions over the entire span of a blade without end-plate at a Reynolds number $Re_c = 7.5 \times 10^6$ (black markers) and with detached end-plates at a gap width $\Delta/c = 0.01$ at a Reynolds number $Re_c = 7.5 \times 10^5$ (red markers), $Re_c = 7.5 \times 10^6$ (green markers) and $Re_c = 7.5 \times 10^7$ (blue markers).

lines and the detached end-plate vorticity lines.

4. Conclusion

Three-dimensional steady-state RANS simulations of the flow around a finite-span lifting blade with detached end-plates have been conducted. The objective of this work was to investigate the potential benefits of detached end-plates on the lift and the drag coefficients of a stationary blade.

Over a relatively large range of gap widths, the presence of detached end-plates results in an increased lift coefficient and a reduced drag coefficient for the blade. The reason is that the use of detached end-plates modifies the path of the vorticity lines on the blade. Indeed, some of the vorticity lines that are normally shed in the wake near the tips of the blade can interact with the detached end-plates and can be shed at the upper and lower extremities of the detached end-plates. This modification of the vorticity lines' path results in an increased amount of spanwise vorticity in the boundary layer near the tips of the blade suction side, which is associated with an increased circulation, and thus, with an increase of the blade lift.

The results presented in this paper and the physical explanations are also valid for regular attached end-plates, i.e., end-plates that are in contact with the blade tips. It is shown that detached end-plates behave like attached end-plates even if there is a gap between the blade and the detached end-plates. Indeed, as long as the viscous rotational zones associated with the blade and the detached end-plates are in contact with one another, the physical mechanisms responsible for the increase of the lift and the reduction of the drag of the blade are essentially the same for the detached end-plates and the attached end-plates.

Simulations of a blade with different geometries of detached end-plates have also been carried out. It has been shown that the transverse dimensions of the detached end-plates are more important than their streamwise dimensions in terms of increasing the lift forces and reducing the drag forces. It has also been presented that one should design detached end-plates that go below and above the blade in the transverse direction in order to increase the potential of interaction between the blade vorticity lines and the detached end-plate vorticity lines and to maximize the benefits of the detached end-plates on the force coefficients.

The understanding gained in this study is useful for numerous fields of application. For example, the conclusions presented in this paper could be used to develop detached end-plates that could help to improve the performance of vertical-axis turbines and flapping-foil turbines.

Acknowledgments

Financial support from the Natural Sciences and Engineering Research Council of Canada (NSERC) is here gratefully acknowledged along with the computational resources provided by Compute Canada and Calcul Québec.

References

[1] S. E. Widnall, The structure and dynamics of vortex filaments, Annual Review of Fluid Mechanics 7 (1) (1975) 141–165.

[2] P. R. Spalart, Airplane trailing vortices, Annual Review of Fluid Mechanics 30 (1) (1998) 107–138.

[3] W. J. Devenport, M. C. Rife, S. I. Liapis, G. J. Follin, The structure and development of a wing-tip vortex, Journal of Fluid Mechanics 312 (1996) 67–106.

[4] J. S. Chow, G. G. Zilliac, P. Bradshaw, Mean and turbulence measurements in the near field of a wingtip vortex, AIAA journal 35 (10) (1997) 1561 – 1567.

[5] L. R. Zuhal, Formation and near-field dynamics of a wing tip vortex, Ph.D. thesis, California Institute of Technology (2001).

[6] D. Birch, T. Lee, Investigation of the near-field tip vortex behind an oscillating wing, Journal of Fluid Mechanics 544 (2005) 201 – 241.

[7] C. Karakus, H. Akilli, B. Sahin, Formation, structure and development of near-field wing tip vortices, Proceedings of the Institution of Mechanical Engineers, Part G: Journal of Aerospace Engineering 222 (1) (2008) 13 – 22.

[8] C. del Pino, L. Parras, M. Felli, R. Fernandez-Feria, Structure of trailing vortices: Comparison between particle image velocimetry measurements and theoretical models, Physics of Fluids 23 (1) (2011) 013602.

[9] J. Dacles-Mariani, G. G. Zilliac, J. S. Chow, P. Bradshaw, Numerical/experimental study of a wingtip vortex in the near field, AIAA journal 33 (9) (1995) 1561 – 1568.

[10] J. Dacles-Mariani, D. Kwak, G. G. Zilliac, On numerical errors and turbulence modeling in tip vortex flow prediction, International Journal for Numerical Methods in Fluids 30 (1) (1999) 65–82.

[11] A. Uzun, M. Y. Hussaini, C. L. Streett, Large-eddy simulation of a wing tip vortex on overset grids, AIAA Journal 44 (6) (2006) 1229 – 1242.

[12] T. J. Craft, A. V. Gerasimov, B. E. Launder, C. M. E. Robinson, A computational study of the near-field generation and decay of wingtip vortices, International Journal of Heat and Fluid Flow 27 (4) (2006) 684 – 695.

[13] A. Uzun, M. Y. Hussaini, Simulations of vortex formation around a blunt wing tip, AIAA Journal 48 (6) (2010) 1221 – 1234.

[14] J.-E. W. Lombard, D. Moxey, S. J. Sherwin, J. F. A. Hoessler, S. Dhandapani, M. J. Taylor, Implicit Large-Eddy Simulation of a Wingtip Vortex, AIAA Journal 54 (2) (2016) 506 – 518.

[15] S. C. Yen, Y. F. Fei, Winglet dihedral effect on flow behavior and aerodynamic performance of NACA0012 wings, Journal of Fluids Engineering 133 (7) (2011) pp. 9.

[16] J. E. Cooper, I. Chekkal, R. C. M. Cheung, C. Wales, N. J. Allen, S. Lawson, A. J. Peace, R. Cook, P. Standen, S. D. Hancock, G. M. Carossa, Design of a morphing wingtip, Journal of Aircraft 52 (5) (2015) 1394 – 1403.

[17] D. McLean, Understanding aerodynamics: arguing from the real physics, John Wiley & Sons, 2012.

[18] R. Gosselin, Analysis and optimization of vertical axis turbines, Ph.D. thesis, Université Laval (2015).

[19] R. Gosselin, G. Dumas, M. Boudreau, Parametric study of H-darrieus vertical-axis turbines using CFD simulations, Journal of Renewable and Sustainable Energy 8 (5) (2016) 053301.

[20] T. Kinsey, G. Dumas, Three-dimensional effects on an oscillating-foil hydrokinetic turbine, Journal of Fluids Engineering 134 (7) (2012) 071105.

[21] D. Kim, B. Strom, S. Mandre, K. Breuer, Energy harvesting performance and flow structure of an oscillating hydrofoil with finite span, Journal of Fluids and Structures 70 (Supplement C) (2017) 314 – 326.

[22] M. M. A. Bhutta, N. Hayat, A. U. Farooq, Z. Ali, S. R. Jamil, Z. Hussain, Vertical axis wind turbine - a review of various configurations and design techniques, Renewable and Sustainable Energy Reviews 16 (4) (2012) 1926 – 1939.

[23] T. Kinsey, G. Dumas, Computational fluid dynamics analysis of a hydrokinetic turbine based on oscillating hydrofoils, Journal of Fluids Engineering 134 (2) (2012) 021104.

[24] I. Paraschivoiu, Wind Turbine Design: With Emphasis on Darrieus Concept, Polytechnic International Press, 2002.

[25] F. Balduzzi, J. Drofelnik, A. Bianchini, G. Ferrara, L. Ferrari, M. S. Campobasso, Darrieus wind turbine blade unsteady aerodynamics: a three-dimensional navier-stokes CFD assessment, Energy 128 (2017) 550 – 563.

[26] G. Tescione, D. Ragni, C. He, C. J. Simão Ferreira, G. J. W. van Bussel, Near wake flow analysis of a vertical axis wind turbine by stereoscopic particle image velocimetry, Renewable Energy 70 (2014) 47 – 61.

[27] R. Gosselin, G. Dumas, M. Boudreau, Parametric study of H-Darrieus vertical-axis turbines using URANS simulations, in: Paper CFDSC-2013 #178, 21st Annual Conference of the CFD Society of Canada, Sherbrooke, Canada, 2013.

[28] M. Boudreau, G. Dumas, Comparison of the wake recovery of the axial-flow and cross-flow turbine concepts, Journal of Wind Engineering and Industrial Aerodynamics 165 (2017) 137 – 152.

[29] P. Chatelain, M. Duponcheel, S. Zeoli, S. Buffin, D.-G. Caprace, G. Winckelmans, L. Bricteux, Investigation of the effect of inflow turbulence on vertical axis wind turbine wakes, Journal of Physics: Conference Series 854 (1) (2017) 012011.

[30] D. You, M. Wang, P. Moin, R. Mittal, Large-eddy simulation analysis of mechanisms for viscous losses in a turbomachinery tip-clearance flow, Journal of Fluid Mechanics 586 (2007) 177–204.

[31] D. You, M. Wang, P. Moin, R. Mittal, Vortex dynamics and low-pressure fluctuations in the tip-clearance flow, Transactions of the ASME. Journal of Fluids Engineering 129 (8) (2007) 1002 – 1014.

[32] M. Dreyer, J. Decaix, C. Münch-Alligné, M. Farhat, Mind the gap - tip leakage vortex in axial turbines, IOP Conference Series: Earth and Environmental Science 22 (5) (2014) 052023.

[33] M. Dreyer, J. Decaix, C. Münch-Alligné, M. Farhat, Mind the gap: a new insight into the tip leakage vortex using stereo-PIV, Experiments in Fluids 55 (11) (2014) 1849.

[34] J. Decaix, G. Balarac, M. Dreyer, M. Farhat, C. Münch-Alligné, RANS and LES computations of the tip-leakage vortex for different gap widths, Journal of Turbulence 16 (4) (2015) 309–341.

[35] A. Pogorelov, M. Meinke, W. Schröder, Effects of tip-gap width on the flow field in an axial fan, International Journal of Heat and Fluid Flow 61, Part B (2016) 466 – 481.

[36] Siemens®, Star-CCM+® V12 User's Guide, `https://mdx.plm.automation.siemens.com/star-ccm-plus` (2017).

[37] P. R. Spalart, S. R. Allmaras, A one-equation turbulence model for aerodynamic flows, La Recherche Aérospaciale 1 (1994) 5 – 21.

[38] P. R. Spalart, C. L. Rumsey, Effective inflow conditions for turbulence models in aerodynamic calculations, AIAA Journal 45 (10) (2007) 2544 – 2553.

[39] J. S. Chow, G. G. Zilliac, P. Bradshaw, Turbulence Measurements in the Near Field of a Wingtip Vortex, Tech. Rep. NASA-TM-110418 (1997).

[40] M. J. Churchfield, G. A. Blaisdell, A reynolds stress relaxation turbulence model applied to a wingtip vortex flow, Orlando, USA, 2011.

[41] M. J. Churchfield, G. A. Blaisdell, Reynolds stress relaxation turbulence modeling applied to a wingtip vortex flow, AIAA Journal 51 (11) (2013) 2643 – 2655.

[42] J. D. Anderson, Fundamentals of Aerodynamics, 2nd edition, McGraw-Hill, 1991.

[43] R. L. Panton, Incompressible Flow, Wiley, New York, 1996.